Computers & Fluids 57 (2012) 195–207

Contents lists available at SciVerse ScienceDirect

Computers & Fluids

journal homepage: www.elsevier.com/locate/compfluid

A study of various factors affecting Newtonian extrudate swell

Evan Mitsoulis [a,*], Georgios C. Georgiou [b], Zacharias Kountouriotis [b]

[a] School of Mining Engineering & Metallurgy, National Technical University of Athens, Zografou, 157 80 Athens, Greece
[b] Department of Mathematics and Statistics, University of Cyprus, P.O. Box 20537, 1678 Nicosia, Cyprus

ARTICLE INFO

Article history:
Received 14 June 2011
Received in revised form 27 September 2011
Accepted 22 December 2011
Available online 31 December 2011

Keywords:
Extrudate swell
Exit correction
Extrusion
Inertia
Gravity
Surface tension
Compressibility
Wall slip
Pressure-dependence of viscosity
Newtonian fluid

ABSTRACT

Finite-element simulations have been undertaken for the benchmark problem of extrudate swell present in extrusion. Both cases of planar and axisymmetric domains were considered under laminar, isothermal, steady-state conditions for Newtonian fluids. The effects of inertia, gravity, compressibility, pressure-dependence of the viscosity, slip at the wall, and surface tension are all considered *individually* in parametric studies covering a wide range of the relevant parameters. The present results extend previous ones regarding the shape of the extrudate and in particular the swelling ratio. In addition, the excess pressure losses in the system (exit correction) were computed. The effect of the domain length is also studied and is found to be of importance in all cases, except for slip and surface tension effects. The effect of the extrudate length is particularly important for inertia and gravity flows. Inertia reduces the swelling down to the asymptotic theoretical values at infinite Reynolds numbers. Gravity acting in the direction of flow also reduces exponentially the swelling. When the flow is creeping and gravity is zero, surface tension, slip at the wall, and pressure-dependence of viscosity, all decrease the swelling monotonically, while compressibility increases it after a small initial reduction. The exit correction decreases monotonically with inertia, gravity, and slip, increases monotonically with compressibility and pressure-dependence of the viscosity, and is not affected by surface tension.

1. Introduction

Extrudate swell ("die swell") is a well-known phenomenon exhibited by viscous fluids exiting long slits or capillary dies [1]. Within the context of non-Newtonian fluid mechanics, this type of flow is of interest in polymer processing, and in particular in the flow of polymer melts in extrusion [2]. Numerical solutions of the extrudate-swell problem were provided in the mid-1970s by a number of researchers [3–5], starting with the pioneering work of Tanner [3], who for the first time calculated correctly the extrudate position. These works dealt primarily with Newtonian fluids and showed how the extrudate surface develops under various conditions, in agreement with experiments [3–6]. The 1980s and 1990s saw a major effort to calculate extrudate swell with viscoelastic models, and these efforts are summarized in various review papers and monographs [1,7–9].

Although the problem is well understood from the physics and fluid mechanics points of view, it has become evident from available numerical simulations that the flow changes considerably when using different constitutive equations or domain geometry (planar vs. axisymmetric). Changing the constitutive equation may lead to a flow that is dramatically different, in very interesting and unpredictable ways [10–14]. The same is true for other parameters influencing the fluid mechanics of extrudate swell flow, ranging from inertia [6,15,16], to gravity [17], to surface tension [6,15,18,19], etc.

A key work by Georgiou et al. [20], which appeared as a short note, showed both computationally and in comparison with experiments that inertia, gravity and surface tension have a pronounced effect on the extrudate shape, reducing it appreciably when gravity acts in the flow direction. Subsequently, Georgiou and co-workers [21–25] have addressed the influence of some standard fluid mechanics parameters on extrudate swell, but again not in full parametric studies. Furthermore, the discussion of pressure results, and hence the excess pressure losses associated with exit flow, which are an integral and important part of the solution, have been neglected.

It is, therefore, the purpose of the present paper to revisit the steady-state Newtonian extrudate-swell problem in both planar and axisymmetric geometries for a full parametric study of the effects of inertia, gravity, compressibility, a pressure-dependent viscosity, slip at the wall, and surface tension on the free surface. The range of parameters will be from the base case of creeping flow without any other effects to the other extreme dictated either from physical arguments or loss of convergence. The emphasis will be

* Corresponding author.
E-mail address: mitsouli@metal.ntua.gr (E. Mitsoulis).

0045-7930/$ - see front matter © 2011 Elsevier Ltd. All rights reserved.
doi:10.1016/j.compfluid.2011.12.019

on providing detailed results both for the free surface location (extrudate swell) and the excess pressure losses in the system (exit correction) as a function of the relevant fluid mechanics dimensionless parameters, as it was done recently for the benchmark fountain flow problem in injection moulding [26].

2. Mathematical modelling

2.1. Governing equations

The geometry of the axisymmetric extrudate-swell problem is shown schematically in Fig. 1, along with the boundary conditions. Cylindrical coordinates are the natural choice, and the gravitational acceleration vector, $\bar{g}$, is assumed to be in the direction of flow. Moreover, the flow is assumed to be isothermal and steady-state [1,27,28]. The flow is governed by the continuity and momentum equations:

$$\nabla \cdot (\rho \bar{u}) = 0, \tag{1}$$

$$\rho \bar{u} \cdot \nabla \bar{u} = -\nabla p + \nabla \cdot \bar{\bar{\tau}} + \rho \bar{g}, \tag{2}$$

where ρ is the density, $\bar{u}$ is the velocity vector, p is the pressure, and $\bar{\bar{\tau}}$ is the extra-stress tensor. Assuming that the fluid is dense with a zero dilatational (bulk) viscosity [1,2], the viscous stress tensor for a compressible Newtonian fluid is given by:

$$\bar{\bar{\tau}} = \mu(\nabla \bar{u} + \nabla \bar{u}^T) - \frac{2\mu}{3}(\nabla \cdot \bar{u})\bar{\bar{I}}, \tag{3}$$

where μ is the viscosity and $\bar{\bar{I}}$ is the unit tensor. Both the density and the viscosity are assumed to be pressure-dependent. The following linear equation of state is considered [29]:

$$\rho = \rho_0[1 + \beta(p - p_0)], \tag{4}$$

where β is the isothermal compressibility assumed to be constant, and ρ_0 is the density at the reference pressure p_0.

Similarly, the viscosity can be a function of pressure, either linear or exponential [30,31]. In the present work, the latter form is employed:

$$\mu = \mu_0 \exp[\beta_p(p - p_0)], \tag{5}$$

where β_p is the constant pressure-shift coefficient, and μ_0 is the viscosity at the reference pressure p_0.

The constitutive equation for Newtonian fluids (Eq. (3)) is substituted into the momentum equations (Eq. (2)), and the equation of state (Eq. (4)) into both the continuity (Eq. (1)) and momentum equations. The resulting system of partial differential equations is closed by appropriate boundary conditions.

2.2. Boundary conditions

As already mentioned, the solution domain and boundary conditions for the axisymmetric geometry are shown in Fig. 1. The boundary conditions are as follows:

(a) Along the axis of symmetry AB, we take the standard symmetry conditions of zero radial velocity and shear stress ($u_r = 0$, $\tau_{rz} = 0$).

(b) Along the wall DS we assume that the normal velocity is zero (no penetration) and that the tangential velocity obeys a linear slip equation [21,32], i.e.,

$$\bar{n} \cdot \bar{u} = 0, \quad \bar{t} \cdot \bar{u} = \beta_{sl}(\bar{t}\bar{n} : \bar{\bar{\tau}}), \tag{6}$$

where β_{sl} is the slip coefficient, and $\bar{n}$ and $\bar{t}$ are the normal and tangential unit vectors to the wall. For straight walls used here, these conditions translate to the radial velocity being zero ($u_r = 0$) and the axial velocity being proportional to the wall shear stress τ_w ($u_z = \beta_{sl}\tau_w$). It should be noted that the no-slip case ($u_z = u_r = 0$) is recovered as β_{sl} goes to zero.

(c) Along the free surface SC (becoming SC′) the kinematic condition $\bar{n} \cdot \bar{u} = 0$ ensures that the free surface is a streamline. Moreover, the tangential stresses vanish ($(\bar{\bar{\sigma}} \cdot \bar{n}) \cdot \bar{t} = 0$), while the normal stresses satisfy a force equilibrium according to [23–25]:

$$(\bar{\bar{\sigma}} \cdot \bar{n}) \cdot \bar{n} = -2R_c\gamma - p_0, \tag{7}$$

where $\bar{\bar{\sigma}} = -p\bar{\bar{I}} + \bar{\bar{\tau}}$ is the total stress, γ is the surface tension, p_0 is the reference pressure (set to 0), and $2R_c$ is the mean curvature of the free surface given by [23–25]:

$$-2R_c = \frac{h_{zz}}{[1 + h_z^2]^{3/2}} - \frac{\alpha}{r\sqrt{1 + h_z^2}}. \tag{8}$$

In the above, the subscripts z and zz denote first- and second-order differentiation of the free surface location h with respect to z, and r is the local radius. The parameter α is an auxiliary one, being 0 for planar flows and 1 for axisymmetric flows. Thus, the second term is 0 in planar flows. It is also clear that in the case of zero surface tension, the normal stress on the free surface vanishes.

(d) Along the outflow plane BC (becoming BC′), taken sufficiently far downstream from the exit so that the flow is uniform, the radial velocity is zero ($u_r = 0$) and the normal stress is given by

$$\sigma_{zz} = -\frac{\alpha\gamma}{h_f}, \tag{9}$$

where h_f is the final radius at the outlet (distance BC′). Note that the normal stress in the case of planar flow is zero (i.e., the surface tension has no effect on the normal stress on the outflow plane).

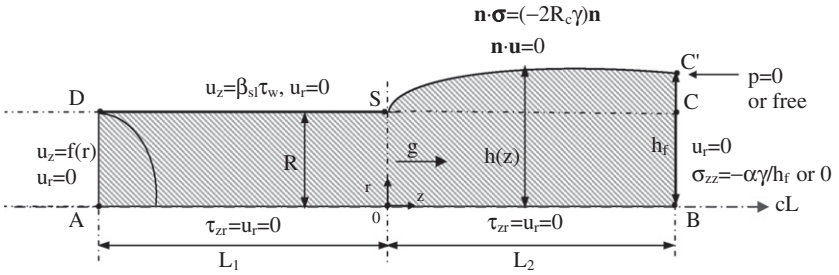

Fig. 1. Schematic diagram of flow domain and boundary conditions for extrusion flow from a die and the accompanying phenomenon of extrudate swell. The constant $\alpha = 0$ for the planar case and $\alpha = 1$ for the axisymmetric one.

(e) Finally, the inlet plane AD is taken sufficiently far upstream from the exit so that the flow is fully developed; the radial velocity is zero ($u_r = 0$), and the axial velocity is given by the Poiseuille incompressible flow solution (with slip in the general case) corresponding to a unit average velocity U [21]. Thus, the inlet profile is not corrected for compressibility or a pressure-dependence of the viscosity.

Previous numerical experiments [26] for setting a reference pressure as a *boundary condition* showed that the best solution is obtained by not specifying anywhere a reference pressure. Especially, in the case of surface tension effects (see below), setting $p = 0$ at C′ or B leads to highly polluted results. However, in the equations the reference pressure p_0 is set to 0.

2.3. Dimensionless equations

To render the Navier–Stokes equations dimensionless, lengths are scaled with the radius R of the tube (or the slit half-width, H, in the planar case), the velocity with the average velocity at the inlet U, and all pressures and stresses with $\mu U/R$ (or $\mu U/H$ in the planar case). Furthermore, the density ρ is scaled with ρ_0 and the viscosity μ is scaled with μ_0. The unit vector in the flow direction is denoted as $\bar{e}$.

Then the governing equations and boundary conditions become:

$$\nabla \cdot (\rho \bar{u}) = 0, \tag{10}$$

$$Re\bar{u} \cdot \nabla \bar{u} = -\nabla p + \nabla \cdot \bar{\bar{\tau}} + St\bar{e}, \tag{11}$$

$$\bar{\bar{\tau}} = \left(\nabla \bar{u} + \nabla \bar{u}^T\right) - \frac{2}{3}(\nabla \cdot \bar{u})\bar{\bar{I}}, \tag{12}$$

$$\bar{\bar{\sigma}} = (\nabla \bar{u} + \nabla \bar{u}^T) - p\bar{\bar{I}}, \tag{13}$$

$$\rho = 1 + Bp, \tag{14}$$

$$\mu = \exp(B_p p), \tag{15}$$

$$\bar{t} \cdot \bar{u} = B_{sl}(\bar{t}\bar{n} : \bar{\bar{\tau}}), \quad \bar{n} \cdot \bar{u} = 0, \tag{16}$$

$$(\bar{\bar{\sigma}} \cdot \bar{n}) \cdot \bar{n} = -2R_c/Ca, \quad (\bar{\bar{\sigma}} \cdot \bar{n}) \cdot \bar{t} = 0, \tag{17}$$

$$\sigma_{zz} = -\frac{\alpha}{Cah_f}. \tag{18}$$

Therefore, four dimensionless numbers appear in the governing equations and another two in the boundary conditions:

(1) The Reynolds number, Re, is a measure of inertia forces over viscous forces:

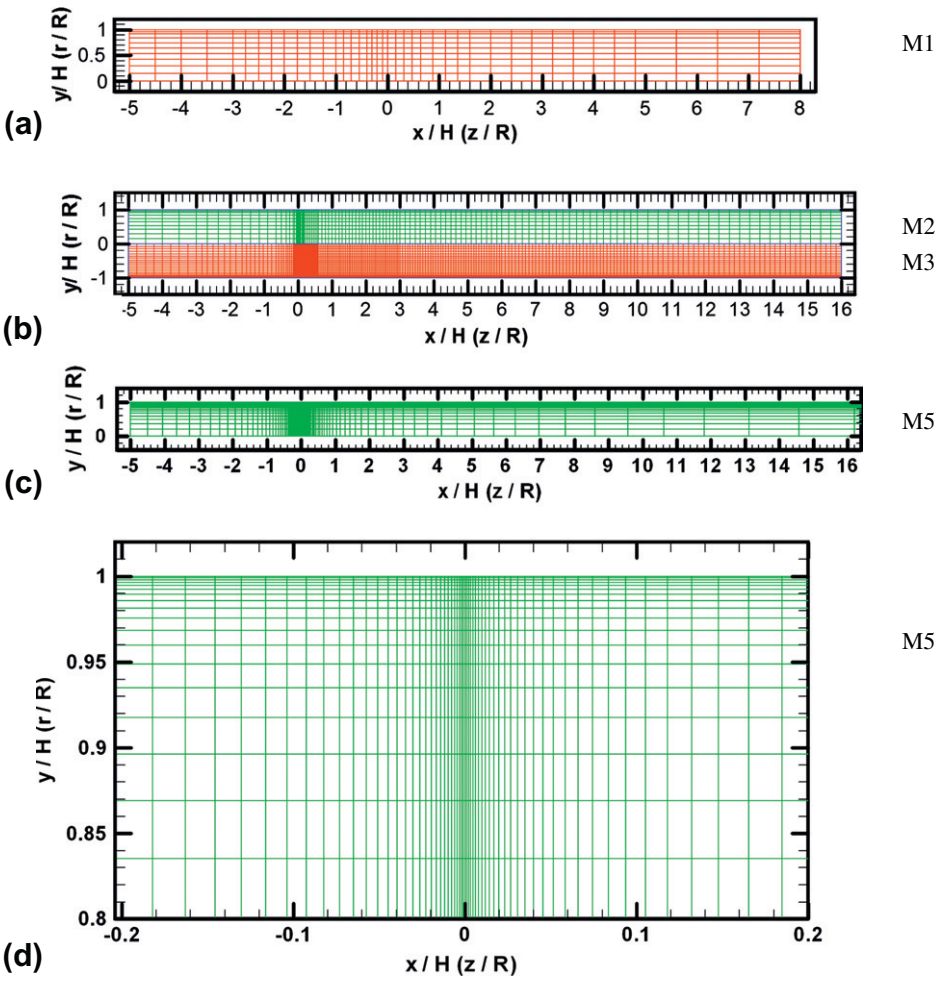

Fig. 2. Finite element meshes used in the current computations: (a) M1, (b) upper half shows M2, while lower half shows M3, (c) M5, (d) blow-up near the die exit of M5. The size of the corner element at the die exit is progressively smaller, being 0.001 for M5. The meshes shown use a flat surface as an initial guess for the extrudate free surface. Table 1 gives the various mesh characteristics.

$$Re = \frac{\rho UR}{\mu}. \tag{19}$$

When $Re = 0$, we have inertialess flow.

(2) The Stokes number, St, is a measure of gravity forces over viscous forces:

$$St = \frac{\rho g R^2}{\mu U}. \tag{20}$$

When $St = 0$, we have no gravity effects.

(3) The compressibility coefficient, B, is a measure of fluid compressibility:

$$B = \frac{\beta \mu U}{R}. \tag{21}$$

When $B = 0$, we have incompressible flow.

(4) The pressure-shift coefficient, B_p, is a measure of pressure-dependence of the fluid viscosity:

$$B_p = \frac{\beta_p \mu U}{R}. \tag{22}$$

When $B_p = 0$, we have no pressure-dependence of the viscosity.

(5) The slip coefficient, B_{sl}, is a measure of fluid slip at the wall:

$$B_{sl} = \frac{\beta_{sl} \mu}{R}. \tag{23}$$

When $B_{sl} = 0$, we have no-slip conditions. When $B_{sl} \approx 1$, we have macroscopically obvious slip.

(6) The capillary number, Ca, is a measure of viscous over surface tension forces:

$$Ca = \frac{\mu U}{\gamma}. \tag{24}$$

When $Ca \to \infty$, viscous forces dominate, as is the case with very viscous fluids. When $Ca \to 0$, surface tension dominates, as is the case with very low-viscosity fluids.

It should be emphasized that in the above the viscosity μ is a constant in all cases except in the case of a pressure-dependence of the viscosity, where it is given by Eq. (15).

3. Method of solution

The above system of governing equations and boundary conditions is solved numerically with the Finite Element Method (FEM), using as primary variables the two velocity components (u and v), the pressure (p), and the free-surface location (h). This is a standard u–v–p–h formulation [20], employing biquadratic basis functions for the velocities, quadratic for h, and bilinear for the pressure. Regarding the iterative algorithms, we have used both Picard (direct substitution) and full-Newton (Newton–Raphson) schemes. The initial mesh configuration was that of a rectangular domain with the exit at 0 plus the extra elements making up the extrudate region.

The domain discretization into finite elements was based on previous experience with extrudate swell calculations and the knowledge that the results for Newtonian fluids converge even with relatively sparse grids [23]. Thus, we have used the grids shown in Fig. 2, designated as M1, M2, M3, M5, with their characteristics given in Table 1, regarding number of nodes on the free surface, elements, nodes and degrees of freedom (dof). Meshes M4 and M5 were carefully refined in the neighbourhood of the singularity, with the size of the smallest element being 0.0025 and 0.001, respectively. FEM results for surface tension were also obtained with the M4 and M5 meshes, which employ a geometric ratio in sizing elements away from the exit singularity. M1 was used here for early trial runs to check the results and gain experience with the different flow parameters. All meshes have an entry length $L_1 = 5R$, which is quite adequate for Newtonian flows to accommodate nonlinear phenomena, that need some length to develop (such as convective flows). The exit is set at 0 for ease of reporting the extrudate location. The adequacy of the entry length was also checked at each run by plotting the centerline velocity profile and observing its levelling off in the region near the entry.

Table 2
Domain lengths used in the simulations for different parameters in extrudate swell of Newtonian fluids.

Dimensionless number	Domain lengths for different parameters	
	$[L_1, L_2]$	Significance[a]
Re	[−5, + 20], [−5, + 100], [−5, + 500]	L_1 NVS, L_2 VS
St	[−5, + 100]	L_1 NVS, L_2 VS
B	[−5, + 16]	L_1 VS, L_2 NVS
B_p	[−5, + 16]	L_1 VS, L_2 NSV
B_{sl}	[−5, + 16]	L_1 NVS, L_2 NVS
Ca	[−5, + 16]	L_1 NVS, L_2 NVS

[a] NSV = not very significant, VS = very significant.

For all of the above cases, we have used a direct substitution iterative scheme (Picard iterations) with a zero-order continuation in a parameter (Re, St, B, B_p, B_{sl}, Ca). The domain lengths used in the simulations, together with their significance, are given in Table 2 for the various parameter ranges. The criteria for termination of the iterative process were for both the norm-of-the-error and the norm-of-the-residuals $<10^{-3}$, and for the maximum free surface change $<10^{-5}$. For the case of surface tension effects, results were also obtained with another code [20] using the Newton–Raphson iterative scheme, which shows a quadratic convergence within 4–5 iterations/Ca.

The solution for extended ranges of parameters needed a careful continuation strategy. Namely, when a parameter step was too big, convergence was lost and we had to use a smaller step to achieve convergence. With this strategy, we were able to reach extended ranges of the relevant parameters. The number of iterations for the Newtonian, creeping, incompressible, base case was 9 (planar) and 10 (axisymmetric) with no under-relaxation used when using the Picard scheme, while with Newton–Raphson the number of iterations were 4–5 to reach machine accuracy. Convergence for most runs was fast and good for a wide range of parameters as shown in Table 3, except near the limiting values, as will be discussed below, especially for surface tension effects.

4. Results and discussion

In order to investigate the effects of the different parameters, we set as the base the flow for $Re = St = B = B_p = B_{sl} = 0$ and

Table 1
Finite element mesh characteristics used in the simulations and Newtonian base results for the extrudate swell ratio, χ, and the exit correction, n_{ex}.

Mesh	No. of FS nodes	No. of elements	No. of nodes	No. of dof	χ (planar)	n_{ex} (planar)	χ (axisym)	n_{ex} (axisym)
M1 (−5,+8)	41	400	1701	3670	1.198	0.153	1.137	0.238
M2 (−5,+16)	201	1200	5061	11,270	1.192	0.151	1.132	0.236
M3 (−5,+16)	401	4800	19,721	44,140	1.191	0.150	1.125	0.232
M4 (−5,+20)*	129	2415	10,063	22,548	1.187	0.146	1.127	0.227
M5 (−5,+20)*	147	3325	13,765	30,866	1.186	0.146	1.127	0.227

* M4 and M5 used with Newton–Raphson iteration.

Table 3
Range of simulations for different parameters in extrudate swell of Newtonian fluids.

Dimensionless number	Limits of parameter range	
	Planar	Axisymmetric
Re	[0–2000]	[0–2000]
St	[0–0.07]	[0–0.07]
B	[0–0.12]	[0–0.24]
B_p	[0–0.05]	[0–0.02]
B_{sl}	[0–100]	[0–100]
Ca	$[\infty$–$10^{-5}]$	$[\infty$–$10^{-5}]$

$Ca = \infty$. The results are given in terms of the (dimensionless) *extrudate swell ratio*, χ, defined by

$$\chi = \frac{h_f}{R} \quad \text{or} \quad \chi = \frac{h_f}{H}. \tag{25}$$

and the dimensionless *pressure* or *exit correction*, n_{ex}, defined by

$$n_{ex} = \frac{\Delta P_w - \Delta P_0}{2\tau_w}, \tag{26}$$

where ΔP_w is the overall pressure drop in the system calculated at the wall, ΔP_0 is the pressure drop based on the fully developed flow in the tube (channel) without the extrudate region, and τ_w is the shear stress for fully developed Poiseuille flow at the tube (channel) wall.

The reasons why these two quantities have been traditionally used for reporting the results are that the extrudate swell ratio is of importance in extrusion for the practitioners, while the excess pressure losses are an indication of how much extra pressure is needed in extrusion due to exit flow [1,2]. Numerically, these values are also a test of the various numerical algorithms used in polymer processing [1].

Tanner [1] provided a selection of χ values from the literature and estimated the extrapolated values as: $\chi = 1.190 \pm 0.002$ (planar) and $\chi = 1.127 \pm 0.003$ (axisymmetric) for an infinite numbers of dof. The converged results obtained by Georgiou and Boudouvis [23] are 1.186 and 1.127. The exit correction n_{ex} is obtained from the wall pressure values given by the simulations at the entry of the domain upstream according to Eq. (26). This is a very sensitive quantity and reflects the adequacy of the domain length, the imposed entry profile, and the finite element mesh used [29]. The creeping values are 0.146 (planar) and 0.227 (axisymmetric) [29]. The present results with different grids are listed in Table 1.

4.1. Inertial flows – effect of Re

The calculations are pursued for increasing Reynolds numbers up to the limiting values of the laminar regime ($0 \leqslant Re \leqslant 2000$), in both planar and axisymmetric geometries. Convergence was good and fast for all cases and no under-relaxation was necessary. However, the problem with inertia flows is the domain length L_2 in the extrudate region, which must be increased accordingly as *Re* increases. As indicated by Georgiou et al. [20], $L_2 = 25$ was adequate for $Re \leqslant 20$, $L_2 = 100$ for $Re \leqslant 100$, and $L_2 = 500$ for $Re \leqslant 2000$. However, in the course of the current work a better rule was found that $L_2 = Re$ for truly adequate lengths. The adequacy of the domain length is shown in Fig. 3, where for the planar geometry, $L_2 = 100$ is adequate for $Re = 100$ but not so for $Re = 200$, as evidenced by the axial velocity u_x plotted along the centerline and the extrudate surface, which do not coincide for $Re = 200$, as they should. Similar graphs were checked for the whole *Re* range. Inadequate domain lengths gave wrong exit corrections, namely values that would not level off but increase as *Re* increased.

An interesting development occurred during the course of the current work with the free or open boundary condition (FBC) of

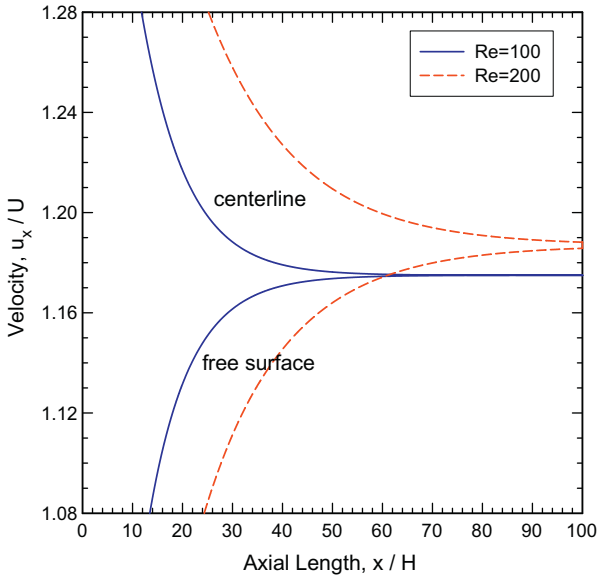

Fig. 3. Axial velocity distribution along the centreline and the free surface for $Re = 100$ and 200. For $Re = 100$, the extrudate length $L_2 = 100$ is adequate and the velocities coincide near the end, while for $Re = 200$, the extrudate length is inadequate and the velocities do not match near the end.

Papanastasiou et al. [33]. The FBC allows the use of truncated domains giving the same results obtained with very long domains. It was applied successfully to this problem and gave results up to $Re = 10{,}000$, with a $L_2 = 6$ [34]. The results for the exit correction up to $Re = 200$ were identical with those from the long domain ($L_2 = 200$), but above that the FBC gave much better and consistent exit correction results, meaning a continuous drop in the exit correction with increasing *Re*. Of course, the swell ratio results are only correct with FBC up to the truncated length, for they continuously drop beyond that truncated domain, and their ultimate value is not known when using FBC.

The free surface shapes are given in [20] and are not repeated here. It is interesting to note that the previous results, although

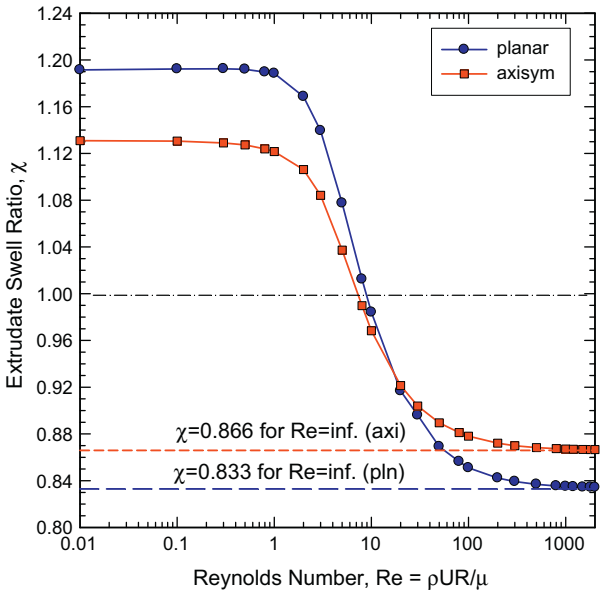

Fig. 4. Extrudate swell ratio χ as a function of the Reynolds number *Re*. Symbols are put here and in the following to show the parameter-continuation steps.

obtained with few elements (222 at most), still give virtually (or visually) the same results as with the current 4800 elements (mesh M3). The results for the extrudate swell ratio χ are shown in Fig. 4, where symbols are put here and in the following graphs to show the parameter-continuation steps. Inertia decreases the χ-values, reaching asymptotically the theoretical limits at infinite *Re* [20]. At $Re \approx 17$, planar and axisymmetric flows have the same $\chi = 0.933$. Below that *Re* value, the planar geometry has a higher swell, and the opposite is true beyond the cross-over point. For the planar geometry, $\chi = 1$ for approximately $Re = 9$, and 0.835 for $Re = 2000$, approaching the theoretical limit 5/6 (0.833) at infinite *Re*; for the axisymmetric geometry, $\chi = 1$ for approximately $Re = 7.3$, and 0.867 for $Re = 2000$, approaching the theoretical limit $\sqrt{3}/2$ (0.866) for infinite *Re* (see Ref. [20] and references therein).

The results for the exit correction n_{ex} are presented in Fig. 5. The effect of inertia is to reduce the n_{ex}-values monotonically and substantially when moving away from the inertialess behaviour. At $Re \approx 2.2$, the planar flows show no extra pressure losses, after which inertia creates a sub-pressure in the field. The same occurs for axisymmetric flows at $Re \approx 3$. The results for $Re \geqslant 200$ have been obtained with the FBC [34] and show a continuous decrease in values (although this is very small) even going up to $Re = 10{,}000$ (not shown).

Therefore, the effect of inertia in the laminar flow range is to decrease monotonically both the extrudate swell and the exit correction in a sigmoidal form, which physically means that inertia forces thrust out the material preventing any swelling and reducing the pressure losses needed for the flow to occur.

4.2. Gravity flows – effect of St

The calculations are then pursued for gravity flows, when gravity acts in the direction of flow (St^+). A similar case was studied by Georgiou et al. [20] (albeit with an added $Re = 0.00725$), who showed that gravity drastically reduces the flow front in agreement with experiments [17], reaching values as low as $\chi \approx 0.543$ at $z/R = 20$ for $St \approx 0.02125$. What is not mentioned in the previous simulations is the domain length L_2, which in the experiments was 71.2*R* [17], and which is a crucial parameter in gravity flows. This subject has been taken up by Housiadas et al. [24] for the annular extrudate-swell problem, who have shown that true results for the extrudate shape are taken only in the first 20–25% of the extrudate length assumed. This comes as a consequence of using a plug velocity profile at exit as a boundary condition, plus the fact that gravity constantly applies an axial force on the fluid, which keeps changing its shape.

Here all results have been obtained with $L_2 = 100$ and are given for this particular extrudate length. The results for the free surface shape for $St = 0.02125$, given in Fig. 5 of [20], were faithfully reproduced in the first 20*R* by using a length $L_2 = 100$ (not shown here). The results for the extrudate swell at $L_2 = 100$ as a function of the Stokes number *St* are given in Fig. 6 for the two geometries. There is an exponential decrease for both cases, where χ reaches low values for relatively low *St* numbers (much lower for the planar case). Convergence for the whole range of simulations was good but relatively slow (slower for the planar case) due to the very long domain used. Severe under-relaxation was needed for the free-surface movement, due to its drastic changes along the extrudate. For the easier axisymmetric case, about 14 iterations at a given *St* were used for *St* up to 0.07 with under-relaxation $\omega = 0.2$. The planar case was much more demanding and needed ω as low as 0.05. The runs were terminated at $St = 0.07$ due to lack of interest.

The results for the exit correction n_{ex} as a function of the Stokes number *St* are given in Fig. 7 for the two geometries. The exit correction decreases monotonically for both cases, more so for the planar case, for which at $St = 0.05$, n_{ex} becomes zero. After that, there is a negative excess pressure loss, meaning that gravity flow has counteracted the pressure-driven flow in the slit die.

It should be noted that when gravity acts in the opposite direction (St^-), a fountain flow occurs at the front, which throws the fluid backwards and is a much more difficult problem to solve [26]. This problem has not been treated here.

It is worth noting here that the FBC is not suitable for gravity flows and is not valid, because the flow phenomena depend always on the domain length, where the gravity force is added [34]. Thus, gravity pulling in the direction of flow always reduces the extrudate swell exponentially and the exit correction substantially, thus requiring less pressure for flow to occur.

4.3. Compressible flows – effect of B

The calculations are then pursued for creeping compressible flows. It should be noted that compressibility has been included

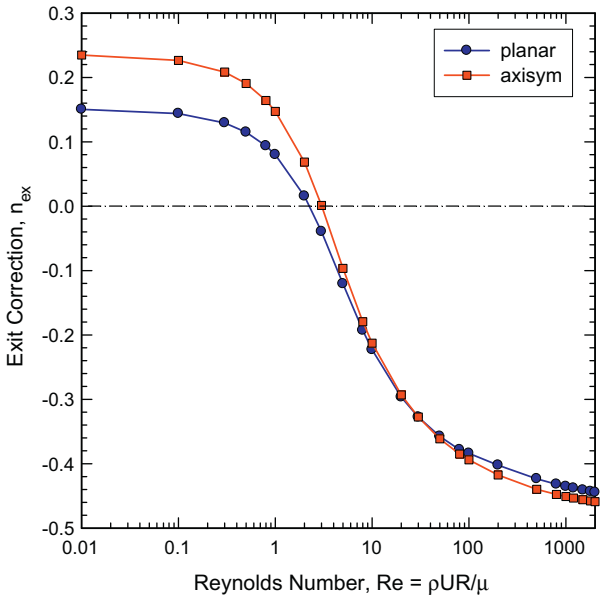

Fig. 5. Exit pressure correction n_{ex} as a function of the Reynolds number *Re*.

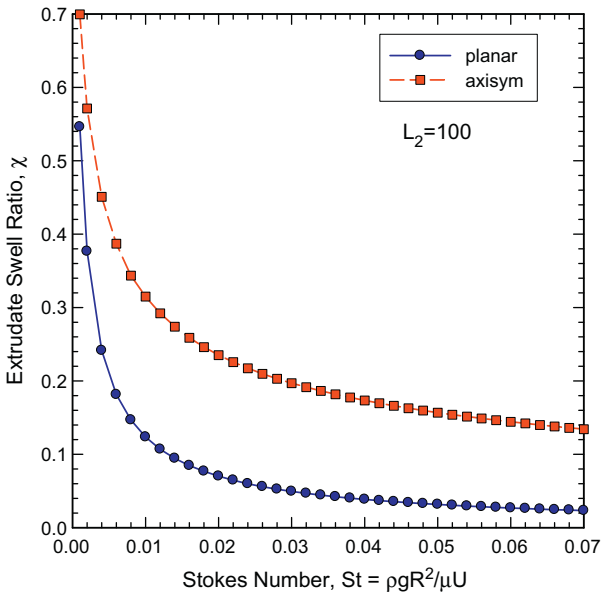

Fig. 6. Extrudate swell ratio χ as a function of the Stokes number *St* when gravity aids the flow.

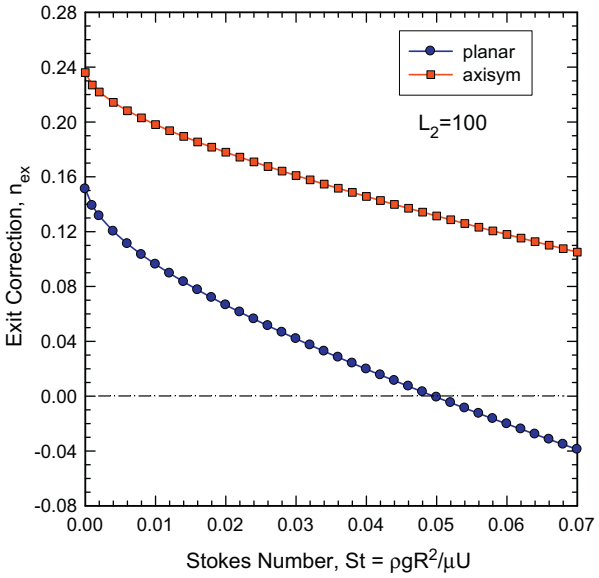

Fig. 7. Exit correction n_{ex} as a function of the Stokes number *St* when gravity aids the flow.

in previous extrudate-swell studies [21,22,29]. Here these results are checked and new results are given for the exit correction based on wall values, which is the customary way of presenting the exit correction (pressure-measuring transducers are placed flush with the wall in practice).

The compressible flow field depends on the domain length L_1, and the results shown here have been produced with a length of 5*R*, which is rather short. Different L_1 lengths have been studied in [29] and are not repeated here. The extrudate domain length is not very important, and a length of $L_2 = 16$ is adequate, at least for a weakly compressible flow [29]. The results for the extrudate-swell ratio χ as a function of the compressibility coefficient *B* are given in Fig. 8 for the two geometries. There is a minimum for both cases (around $B = 0.045$ for the planar flow and $B = 0.025$ for the axisymmetric one), after which χ reaches quickly high values. There is a cross-over point at $B = 0.06$, where $\chi = 1.17$.

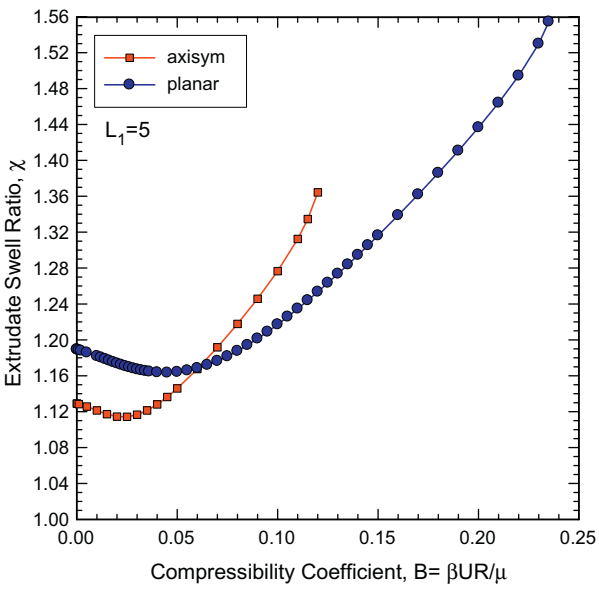

Fig. 8. Extrudate swell ratio χ as a function of the compressibility coefficient *B*.

The axisymmetric case exhibits lower values than the planar one before the cross-over point, after which the opposite holds. Convergence was good and fast (3–7 iterations needed) except for the higher range of *B*, where it was slow and difficult and reached a limiting value of $B_{lim} = 0.12$ (axisymmetric) and 0.24 (planar).

The results for the exit correction n_{ex} as a function of *B* are given in Fig. 9 for the two geometries. The exit correction in the present case has been calculated with pressure values at the wall and by subtracting the pressure drop ΔP_0 in the die calculated without compressibility. Then, the exit correction rises quadratically for both cases to fairly high values, reaching 4 for the axisymmetric case for $B = 0.12$. This was not the case in [26], where ΔP_0 in the die was calculated at the same level of compressibility, thus resulting in much lower n_{ex} values. For completeness, the centreline values of [29] are also presented in Fig. 9. In compressible flows the difference between wall and centreline values is substantial, which is not the case for inertia or gravity flows.

Thus, compressibility has the opposite effect from inertia and gravity, as it serves to increase the extrudate swell and the exit correction substantially. These effects are a consequence of the pressure-dependence of density, which changes appreciably as *B* increases, and the material swells more upon exiting to release the normal forces and it also needs extra pressure to be pushed out of the die.

4.4. Flows with a pressure-dependent viscosity – effect of B_p

The calculations are then pursued for creeping flows with a pressure-dependent viscosity. Studies with pressure-dependent viscosity have been done before [26,30,35,36], realizing the fact that under high pressures exerted in extrusion, the pressure effect on the viscosity cannot be ignored [31,35]. Also in the field of lubrication, this effect is important [30]. However, this is the first time that the effects of the pressure-dependence of the viscosity are investigated in extrudate swell.

As with compressible flows, the results depend on the domain length L_1. Those shown here have been produced with a length of 5*R*. The extrudate length L_2 is not very significant and has been set to 16*R*. The inlet Poiseuille velocity profile is set as the parabolic one for a unit mean velocity. The results for the extrudate-swell

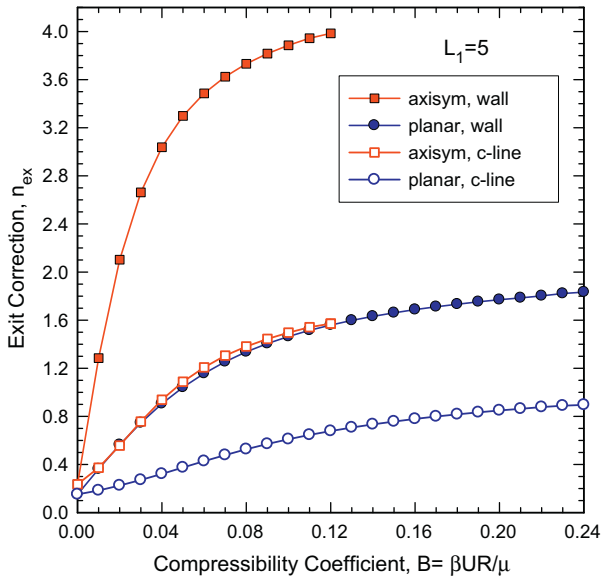

Fig. 9. Exit correction n_{ex} as a function of the compressibility coefficient *B*. The values are calculated both at the wall and at the centreline (*c*-line) [29] to show the differences.

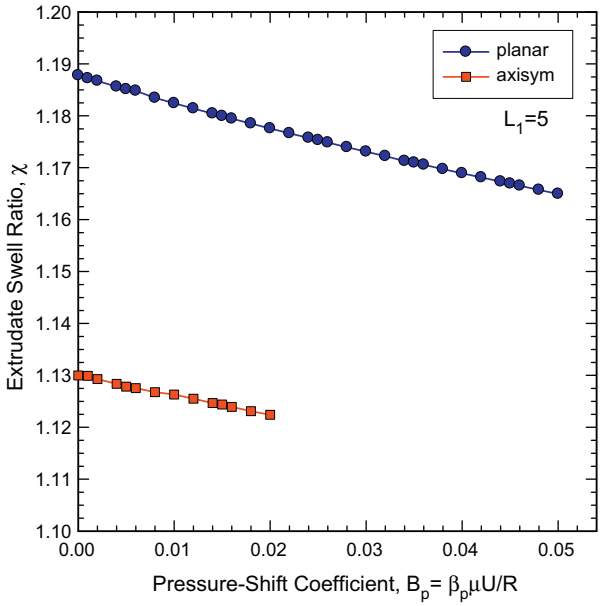

Fig. 10. Extrudate swell ratio χ as a function of the pressure-shift coefficient B_p.

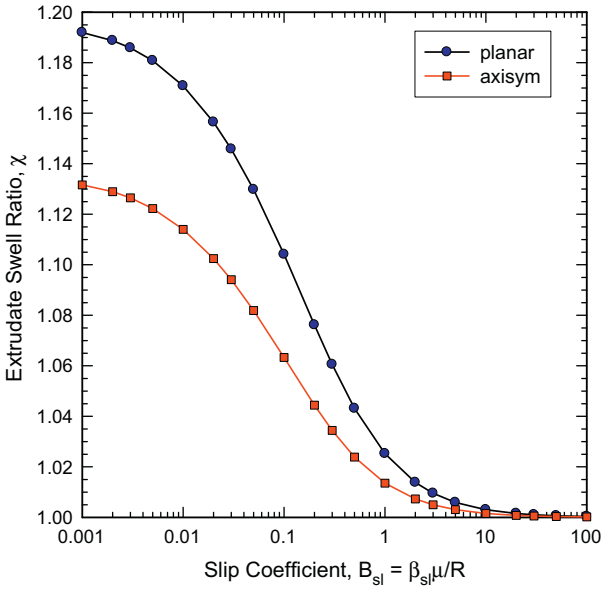

Fig. 12. Extrudate swell ratio χ as a function of the slip coefficient B_{sl}.

ratio χ as a function of the pressure-shift coefficient B_p are given in Fig. 10 for the two geometries. There is a linear decrease for both cases, at least in the range of B_p-numbers studied. For the range of our simulations, the axisymmetric case always exhibits markedly lower values than the planar one. Due to the exponential nature of the pressure-dependence of the viscosity (Eq. (5)), convergence was lost suddenly at low values of B_p ($B_p = 0.05$ for the planar and $B_p = 0.02$ for the axisymmetric case. The longer the L_1 the lower these limiting values become. Up to those B_p-limiting values, convergence was good and fast (four Picard iterations were sufficient for most of the runs). Similar trends were found in the fountain flow problem [26,30].

The results for the exit correction n_{ex} as a function of B_p are given in Fig. 11 for the two geometries. It should be mentioned that the values of ΔP_0 and τ_w appearing in Eq. (17) are those for fully-developed Poiseuille flow with no pressure-dependence of the viscosity. The exit correction rises exponentially for both cases, with the axisymmetric case rising much faster for the same B_p-number.

Thus, for a pressure-dependence of viscosity, the extrudate swell decreases while the exit correction rises exponentially, and this latter behaviour is similar to the compressibility effect. However, the decrease in swell occurs because of the varying viscosity of the material in the flow field according to pressure; namely a lower viscosity in the outer layers of the fluid leads to a decrease in swelling and eventually to a contraction, as has been explained by Tanner [37] and Mitsoulis [38].

We now turn our attention to the effect of dimensionless parameters as they arise from the flow along or across the domain boundaries. These include slip at the solid channel or tube walls (hence the effect of slip parameter, B_{sl}) and surface tension (hence the effect of capillary number, Ca) on the extrudate flow.

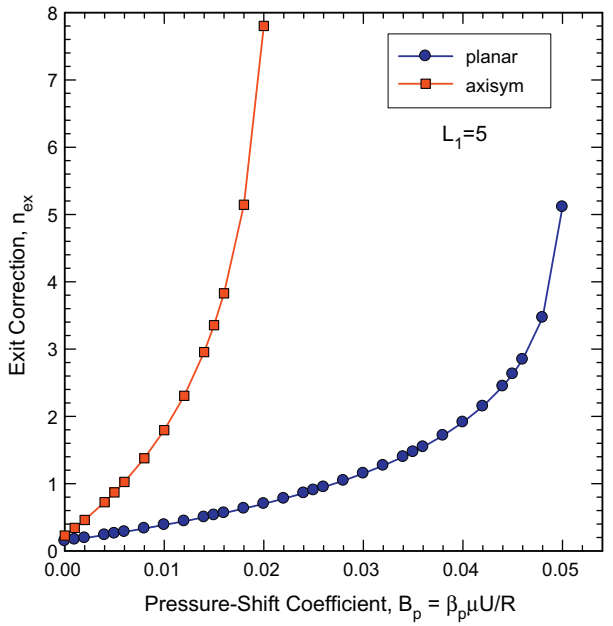

Fig. 11. Exit correction n_{ex} as a function of the pressure-shift coefficient B_p.

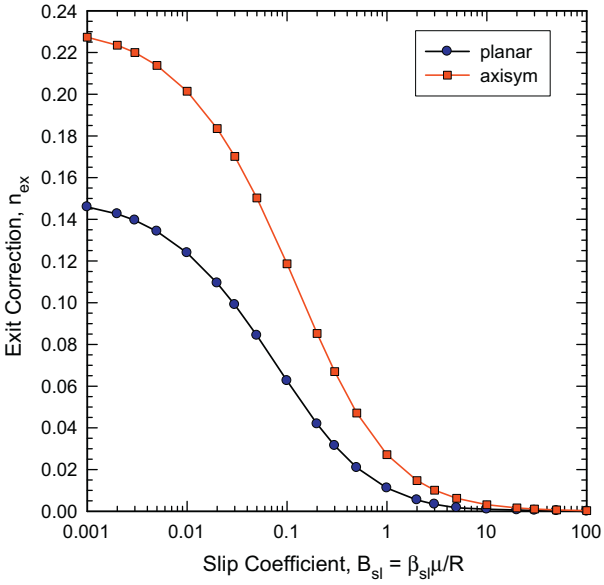

Fig. 13. Exit correction n_{ex} as a function of the slip coefficient B_{sl}.

4.5. Flows with slip at the wall – effect of B_{sl}

The calculations are then pursued for creeping, incompressible flows with slip at the wall. This case has been studied adequately before [15,21,29,32], and it is repeated here for completeness.

The simulations have been pursued for a wide range of B_{sl}-values from 0 (no slip) to 100 (approaching perfect slip for which $B_{sl} \to \infty$). Convergence for this problem was always good and fast, requiring at most 14 Picard iterations in the middle range of B_{sl}–values, where the changes were bigger. No under-relaxation for the free-surface movement was necessary. The results do not depend appreciably on the domain length, so we have used the standard lengths of $L_1 = 5$ and $L_2 = 16$.

The results for the extrudate-swell ratio χ as a function of the slip coefficient B_{sl} are given in Fig. 12 for the two geometries. There is a typical sigmoidal decrease for both cases in the range of B_{sl}-values. Most of the changes occur in the range $0.01 < B_{sl} < 1$. The axisymmetric case exhibits always markedly lower values than the planar one for the whole range of simulations. As B_{sl} increases approaching perfect slip ($B_{sl} \to \infty$), the extrudate swell reaches an asymptotic no swell value ($\chi = 1$), due to the fact that the flow is a plug everywhere.

The results for the exit correction n_{ex} as a function of B_{sl} are given in Fig. 13 for the two geometries. It should be mentioned that the values of ΔP_0 and τ_w appearing in Eq. (26) are those for fully-developed Poiseuille flow with slip according to the analytical solutions based on a linear slip law [29]. The exit correction follows the sigmoidal behaviour of the extrudate swell for both cases, with the axisymmetric case giving always higher values for the same B_{sl}–number. Eventually all values go to 0, as the fluid slips perfectly along the solid walls.

Thus, slip at the wall serves to reduce both the extrudate swell and the exit correction monotonically, and in both cases the values reach asymptotically zero (no swell, no excess pressure losses) for perfect slip, as the material does not adhere to the die walls and flows out with a plug velocity profile.

4.6. Flows with surface tension – effect of Ca

The calculations are then pursued for creeping, incompressible flow of fluids having non-negligible surface tension. This case has been the object of major studies starting with the work by Reddy and Tanner [6] and continued with Omodei's works [18,19], and Silliman and Scriven's [15]. All these works used Picard iterations (successive substitution) and the kinematic boundary condition (KC) ($\bar{n} \cdot \bar{u} = 0$) to solve the system of equations and were plagued by early loss of convergence (for $Ca < 0.5$). This led to some controversies regarding which free-surface boundary conditions to iterate on, namely the kinematic condition vs. the normal stress condition (NSC) (Eq. (17)), with the latter being much better for $Ca < 0.5$ leading to results down to $Ca = 0.01$ [15]. The issue was settled by Ruschak's work [39], who employed a clever integration by parts of the surface tension term in Eq. (17), thus eliminating the explicit appearance of surface curvature in Eq. (8), and allowing a piecewise linear approximation of the surface shape even when surface tension effects are important (see [20] for FEM details). Ruschak [39] used for the first time the Newton–Raphson iterative scheme and was able to get results down to $Ca = 0.01$, with few iterations (4–5) for each Ca number.

Ruschak's method was applied by Georgiou et al. [20], who went down to $Ca = 10^{-5}$ for the extrudate swell problem and reproduced Richardson's analytical results for the *planar* stick–slip

Table 4
Simulations results for different Ca numbers in extrudate swell of Newtonian fluids (results from meshes M4 and M5 with the Newton–Raphson iteration).

Ca	Planar		Axisymmetric	
	χ	n_{ex}	χ	n_{ex}
10^{+5}	1.186	0.146	1.127	0.227
100	1.186	0.147	1.126	0.227
50	1.185	0.147	1.126	0.227
10	1.180	0.146	1.121	0.227
5	1.173	0.146	1.116	0.226
1	1.129	0.145	1.085	0.224
0.5	1.096	0.144	1.064	0.223
0.1	1.031	0.143	1.021	0.221
0.05	1.016	0.143	1.011	0.222
0.01	1.004	0.143	1.002	0.222
0 (stick–slip)	1.000	0.143	1.000	0.222

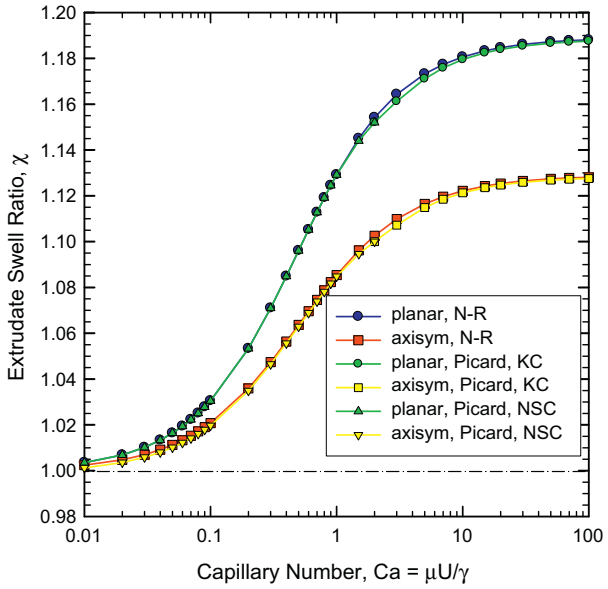

Fig. 14. Extrudate swell ratio χ as a function of the capillary number Ca. N–R = Newton–Raphson iteration, P = Picard iteration, KC = kinematic condition, NSC = normal stress condition.

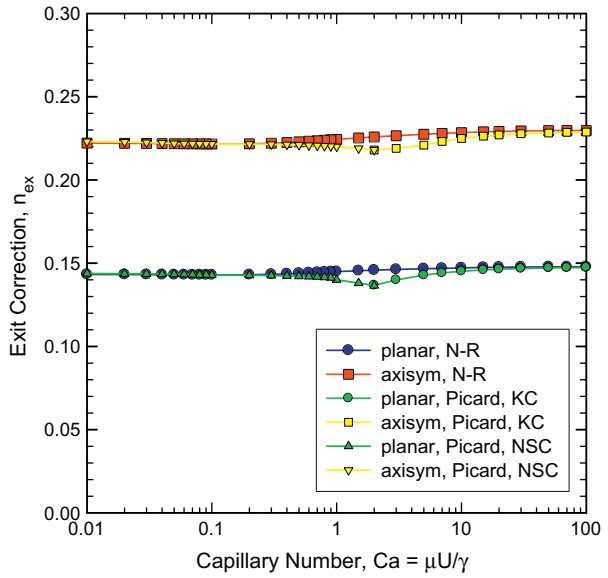

Fig. 15. Exit correction n_{ex} as a function of the capillary number Ca. Results deviating from the constant values reveal inaccuracies in the calculations. N–R = Newton–Raphson iteration, P = Picard iteration, KC = kinematic condition, NSC = normal stress condition.

problem (zero swelling). Since then, Georgiou and his co-workers have applied successfully this method to other cases of extrudate swell with high surface tension effects [23–25]. However, none of these works has addressed the issue of pressure, and hence results for the exit correction are lacking. Also, in previous works the influence of surface tension was sometimes masked by coupling it with gravity and inertia, and therefore its effect was not clear. Here a thorough well-documented range of simulations is undertaken. As was the case with slip, the results do not depend on the domain length, so we have used the standard lengths of

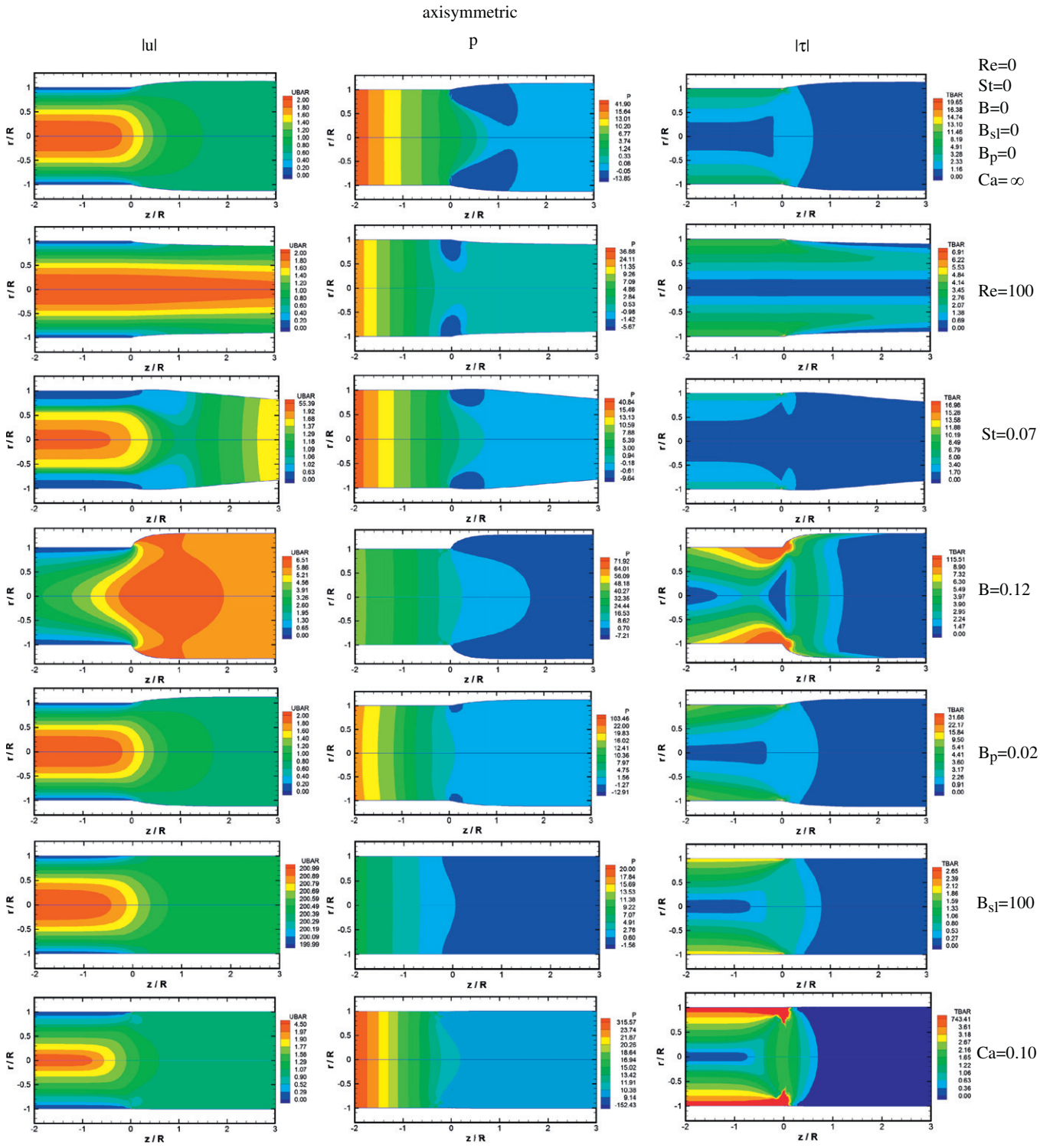

Fig. 16. Contour variables for axisymmetric extrudate swell flow of Newtonian fluids: left column, $|u| = \sqrt{u_r^2 + u_z^2}$ = UBAR, middle column, pressure P, right column, $|\tau| = \sqrt{\frac{1}{2}(\bar{\bar{\tau}} : \bar{\bar{\tau}})}$ = TBAR. The maximum values correspond to the highest number in the legend (red). The minimum values correspond to the lowest number in the legend (blue). Each row represents the parameter effect shown on the right, which is near the limiting value of the parameter range used in the simulations. The graphs are drawn to scale for easy comparisons with the base case (1st row). (For interpretation of the references to colour in this figure legend, the reader is referred to the web version of this article.)

$L_1 = 5$ and $L_2 = 16$, and repeated the runs with $L_2 = 20$ (meshes M4 and M5) with no discernible differences found.

The simulations have been pursued for a wide range of *Ca*-values from ∞ (or a big number, say 100,000) (no surface tension) to 10^{-5} (strong surface tension effects). Ruschak's method has been used for treating the surface tension terms of Eq. (17). Results have been obtained independently with both Picard (*P*) and Newton–Raphson (N–R) iterations. The continuation steps for each method are given in the respective graphs. Convergence for this problem with N–R was good and fast, requiring usually around 5–6

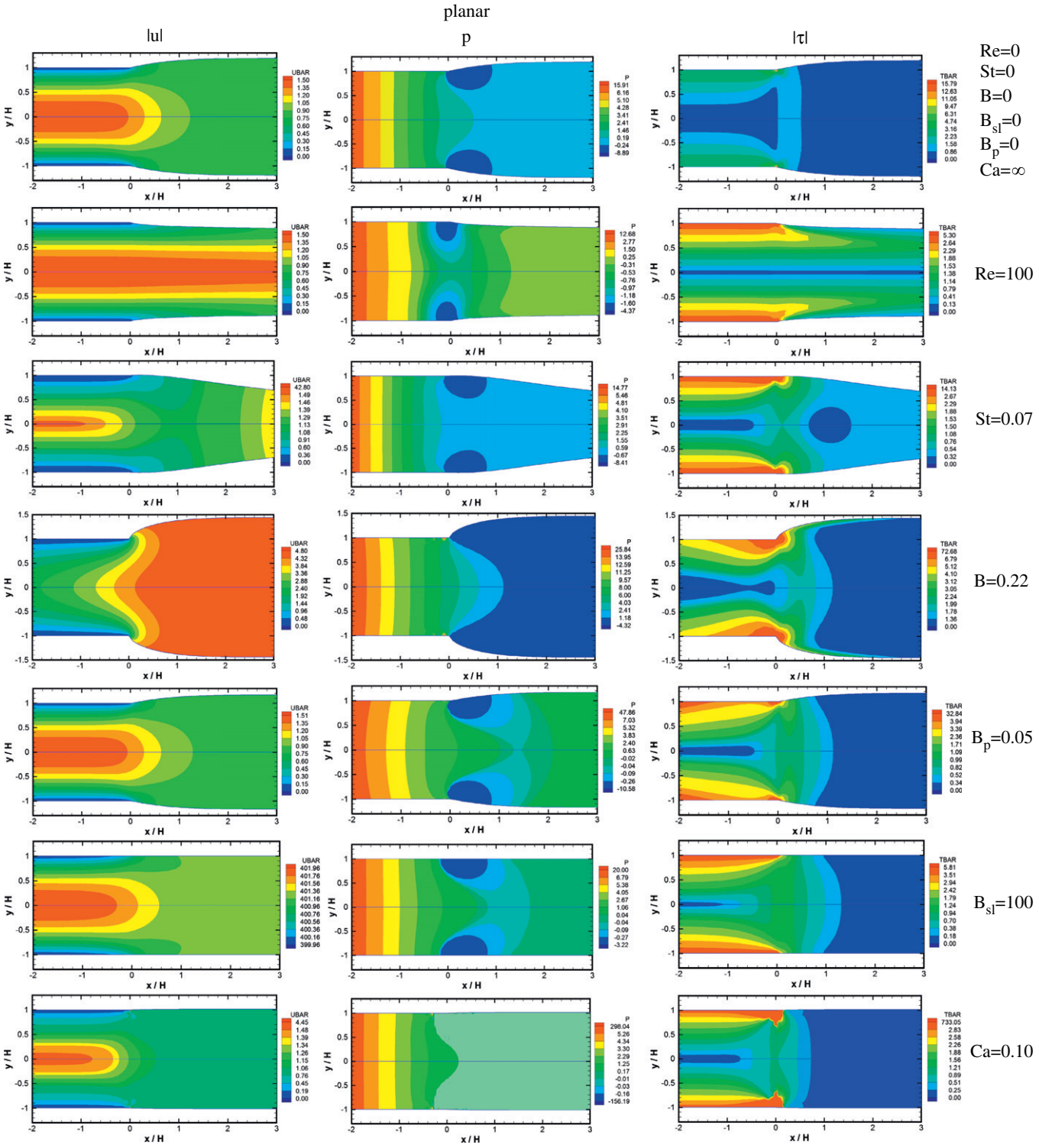

Fig. 17. Contour variables for planar extrudate swell flow of Newtonian fluids: left column, $|u| = \sqrt{u_x^2 + u_y^2}$ = UBAR, right column, pressure *P*, right column, $|\tau| = \sqrt{\frac{1}{2}(\bar{\bar{\tau}} : \bar{\bar{\tau}})}$ = TBAR. The maximum values correspond to the highest number in the legend (red). The minimum values correspond to the lowest number in the legend (blue). Each row represents the parameter effect shown on the right, which is near the limiting value of the parameter range used in the simulations. The graphs are drawn to scale for easy comparisons with the base case (1st row). (For interpretation of the references to colour in this figure legend, the reader is referred to the web version of this article.)

iterations per step. Using the Picard method with the kinematic condition and starting with zero surface tension ($Ca \to \infty$), it was possible to go down to $Ca = 0.02$ (planar) and $Ca = 0.04$ (axisymmetric). However, this was possible using careful continuation steps, many iterations, and severe under-relaxation for the low values of Ca (starting from $\omega = 1$ and going down to $\omega = 0.01$ of the free-surface movement). Furthermore, the results were not accurate for $Ca < 1$. On the other hand, using the Picard method with the normal-stress boundary condition and starting from the stick–slip flow ($Ca = 0$), it was possible to obtain results fast in the other extreme of the range (low Ca values, $Ca < 1$), thus corroborating Silliman and Scriven's findings [15]. In general, using the Picard scheme for this problem proved to be a difficult process, especially around $Ca = 1$, much more difficult than with any of the other five (5) fluid-mechanics parameters studied. It should be emphasized that this was not the case when using the N–R scheme, which showed good and fast convergence for the whole range of Ca values.

An important finding, that is particularly valid in the axisymmetric case and which has never been touched upon before, is the necessity of not having set $P = 0$ at any node in the system. If the pressure is set to 0 at, say, the outlet corner, point B or C in Fig. 1, then the axisymmetric case produces highly polluted results for the pressure, the radial and axial velocity components, and the components of the stress tensor. Then the calculation of the exit correction becomes useless. The pressure is not zero at the outlet, but it takes values which depend on the surface tension (see outflow boundary condition of Eq. (18) and Fig. 1). For example, at $Ca = 10^{-2}$, $P_{in} = 141.535$ and $P_{out} = 99.758$, giving an exit correction of $n_{ex} = 0.222$! This is not the case for planar flows, where $P = 0$ at outlet and also for any other of the fluid-mechanics parameters studied.

The results for the extrudate-swell ratio χ as a function of the capillary number Ca are given in Fig. 14 for the two geometries. The two codes give essentially the same results (with both meshes M4 and M5). Numerical values are also given in Table 4 for reference purposes. There is a typical sigmoidal decrease for both cases in the range of Ca-values studied. This typical behaviour has been also observed in the fountain flow problem [26]. The axisymmetric case exhibits always markedly lower values than the planar one for the whole range of simulations. As Ca decreases approaching zero (strong surface tension effects), the free surface tends to go to zero swell, due to a strong surface tension which does not allow the fluid to swell. The results for the free surface shape and for different Ca numbers are given in [20] (their Fig. 2a), and they are not repeated here.

The new results for the exit correction n_{ex} as a function of Ca are given in Fig. 15 for the two geometries, and in Table 4 in numerical form for reference purposes. A rather interesting and unexpected phenomenon occurs. The exit correction remains almost constant for both cases, starting from the corresponding results of zero surface tension (0.227 for the axisymmetric case and 0.147 for the planar one), and reaching for $Ca = 0$ (stick–slip case) the values of 0.222 and 0.143, respectively. It should be noted that any numerical errors near the singularity manifest themselves in rapidly decreasing exit correction values, while the extrudate swell remains basically unaffected. This is the case with the Picard method when using inappropriate free-surface boundary conditions to iterate upon.

Thus, surface tension reduces the swelling to the case of stick–slip (no swell) as the material is strangled in a sense by severe compressive forces as it comes out of the die. On the other hand, the exit correction remains constant, since these capillary forces are balanced by the pressure forces in the fluid, and therefore no extra pressure drop is needed in the die to extrude the fluid.

4.7. Flow fields

It is instructive to show results for the primary field variables for the various fluid mechanics parameters studied above. This is done in the form of contours in Figs. 16 and 17 (axisymmetric and planar, respectively) for the magnitude of the velocity vector $|u| = \sqrt{u_r^2 + u_z^2}$ = UBAR, the pressure P (isobars), and the magnitude of the extra stress tensor $|\tau| = \sqrt{\frac{1}{2}(\bar{\bar{\tau}} : \bar{\bar{\tau}})}$ = TBAR. The graphs are drawn to scale for easy comparisons. In each case, the limiting value is chosen for depiction, just before divergence occurred or the runs were stopped. The comparisons are made with the base case of ($Re = St = B = B_p = B_{sl} = 0$, $Ca = \infty$), which is given in the first row of Figs. 16 and 17, respectively. In each of these two figures are given the cases of Re, St, B, B_p, B_{sl}, and Ca.

A detailed study of the contours for each case reveals interesting trends, which are not always anticipated. We see, for example, that both inertia (effect of Re, 2nd row of Figs. 16 and 17) and gravity acting in the direction of flow (effect of St, 3rd rows) reduce the free surface substantially, but apart from that the flow field does not show any surprises. Compressibility (effect of B, 4th rows) accelerates the flow towards the die exit and increases the swelling. A pressure-dependent viscosity (effect of B_p, 5th rows) bends the isobars and influences the stresses but not the velocity contours. Slip at the wall (effect of B_{sl}, 6th rows) reduces drastically the changes in the velocity field (almost plug flow), while the pressure and stress values become very small. Surface tension (effect of Ca, 7th rows) shows a shear flow almost up to the die exit, but the pressures and stresses are very high on the free surface, suppressing the swelling.

5. Conclusions

Finite element solutions have been obtained for both the planar and axisymmetric extrudate-swell flows of Newtonian fluids under the individual influence of inertia, gravity, compressibility, slip at the wall, surface tension and pressure-dependence of the viscosity. A linear slip law was assumed. Emphasis was given on calculating the extrudate-swell ratio and the pressure exit correction. The base cases of creeping flow results are highly altered when different forces are at play. Inertia reduces rapidly the swelling as Re increases, and reduces the exit correction. Gravity forces acting in the flow direction cause an even more rapid decrease of extrudate swell for relatively small values of St, while the exit correction also decreases. Compressibility serves to reduce at first the swelling and then increase it substantially, while it increases monotonically the exit correction. An exponentially pressure-dependent viscosity serves to decrease the extrudate swell linearly and increase the exit correction exponentially.

Boundary effects include slip at the wall and surface tension at the free surface. As the slip coefficient B_{sl} increases, both swelling and the exit correction decrease in a sigmoidal fashion and go to 0 as slip becomes dominant. The sigmoidal behaviour is also evident for the extrudate swell as Ca decreases (strong surface tension effects) with the extrudate swell going to unity, while the exit correction remains constant. This last finding is a strong indication of accurate calculations with surface tension effects, since any numerical inaccuracies lead to rapid negative corrections. The best method to calculate flows with surface tension is the FEM with N–R iteration, while FEM with Picard iteration needs careful consideration of the boundary condition to iterate upon (kinematic condition for $Ca > 2$ and normal stress condition for $Ca \leqslant 2$) [15].

Although the present results are limited to Newtonian fluids, the effects discussed apply at least qualitatively to all fluids. Since a variety of fluids undergo extrusion under a wide range of conditions, it is hoped that the present results may be of interest to practitioners in the field of fluid mechanics.

Acknowledgements

The authors are indebted to the ERASMUS program (Subprogram SOCRATES) for scientific visits to Cyprus related to this project.

References

[1] Tanner RI. Engineering rheology. 2nd ed. Oxford, UK: Oxford University Press; 2000.
[2] Tadmor Z, Gogos CG. Principles of polymer processing, SPE monograph series. New York: Wiley; 1979.
[3] Tanner RI. Die-swell reconsidered: some numerical solutions using a finite element program. Appl Polym Symp 1973;20:201–8.
[4] Nickell RE, Tanner RI, Caswell B. The solution of viscous incompressible jet and free-surface flows using finite-element methods. J Fluid Mech 1974;65:189–206.
[5] Tanner RI, Nickell RE, Bilger RW. Finite element methods for the solution of some incompressible non-Newtonian fluid mechanics problems with free surfaces. Comput Meth Appl Mech Eng 1975;6:155–74.
[6] Reddy KR, Tanner RI. Finite element solution of viscous jet flows with surface tension. Comput Fluids 1978;6:83–91.
[7] Keunings R. Progress and challenges in computational rheology. Rheol Acta 1990;29:556–70.
[8] Mitsoulis E. Numerical simulation of viscoelastic fluids. In: Cheremisinoff NP, editor. Encyclopedia of fluid mechanics, polymer flow engineering, vol. 9. Dallas, Texas, USA: Gulf Publ. Co.; 1990. p. 649–704.
[9] Owens RG, Phillips TN. Computational rheology. London: Imperial College Press; 2002.
[10] Luo X-L, Mitsoulis E. Memory phenomena in extrudate swell simulations from annular dies. J Rheol 1989;33:1307–27.
[11] Mitsoulis E. Extrudate swell of Boger fluids. J Non-Newtonian Fluid Mech 2010;165:812–24.
[12] Russo G, Phillips TN. Numerical simulation of steady planar die swell for a Newtonian fluid using the spectral element method. Comput Fluids 2010;39:780–92.
[13] Russo G, Phillips TN. Spectral element predictions of die-swell for Oldroyd-B fluids. Comput Fluids 2011;43:107–18.
[14] Russo G, Phillips TN. Numerical prediction of extrudate swell of branched polymer melts. Rheol Acta 2010;49:657–76.
[15] Silliman WJ, Scriven LE. Separating flow near a static contact line: slip at a wall and shape of a free surface. J Comput Phys 1980;34:287–313.
[16] Gear RL, Keentok M, Milthorpe JF, Tanner RI. The shape of low Reynolds number jets. Phys Fluids 1983;26:7–9.
[17] Trang CT, Yeow YL. Extrudate swell of Newtonian and non-Newtonian fluids-the effect of gravitational body force. J Non-Newtonian Fluid Mech 1986;20:103–16.
[18] Omodei BJ. Computer solutions of a plane Newtonian jet with surface tension. Comput Fluids 1979;7:79–96.
[19] Omodei BJ. On the die-swell of an axisymmetric Newtonian jet. Comput Fluids 1980;8:275–89.
[20] Georgiou GC, Papanastasiou TC, Wilkes JO. Laminar Newtonian jets at high Reynolds number and high surface tension. AIChE J 1988;34:1559–62.
[21] Georgiou GC, Crochet MJ. Time-dependent extrudate-swell problem with slip at the wall. J Rheol 1994;38:1745–55.
[22] Georgiou GC. The compressible Newtonian extrudate swell problem. Int J Numer Meth Fluids 1995;20:255–61.
[23] Georgiou GC, Boudouvis AG. Converged solutions of the Newtonian extrudate-swell problem. Int J Numer Meth Fluids 1999;29:363–71.
[24] Housiadas K, Georgiou G, Tsamopoulos J. The steady annular extrusion of a Newtonian liquid under gravity and surface tension. Int J Numer Meth Fluids 2000;33:1099–119.
[25] Georgiou G. Annular liquid jets at high Reynolds numbers. Int J Numer Meth Fluids 2003;42:117–30.
[26] Mitsoulis E. Fountain flow revisited: the effect of various fluid mechanics parameters. AIChE J 2010;56:1147–62.
[27] Barnes HA, Hutton JF, Walters K. An introduction to rheology, rheology series. Amsterdam: Elsevier; 1989.
[28] Mitsoulis E. Annular extrudate swell of pseudoplastic and viscoplastic fluids. J Non-Newtonian Fluid Mech 2007;141:138–47.
[29] Taliadorou E, Georgiou GC, Mitsoulis E. Numerical simulation of the extrusion of strongly compressible Newtonian liquids. Rheol Acta 2008;47:49–62.
[30] Huilgol RR, You Z. On the importance of the pressure dependence of viscosity in steady non-isothermal shearing flows of compressible and incompressible fluids and in the isothermal fountain flow. J Non-Newtonian Fluid Mech 2006;136:106–17.
[31] Cardinaels R, Van Puyvelde P, Moldenaers P. Evaluation and comparison of routes to obtain pressure coefficients from high-pressure capillary rheometry data. Rheol Acta 2007;46:495–505.
[32] Mitsoulis E. Annular extrudate swell of Newtonian fluids: effects of compressibility and slip at the wall. J Fluids Eng 2007;129:1384–93.
[33] Papanastasiou TC, Malamataris N, Ellwood K. A new outflow boundary condition. Int J Numer Meth Fluids 1992;14:587–608.
[34] Mitsoulis E, Malamataris NA. Free (open) boundary condition: some experiences with viscous flow simulations. Int J Numer Meth Fluids 2011. doi:10.1002/fld.2608.
[35] Ansari M, Alabbas A, Hatzikiriakos SG, Mitsoulis E. Entry flow of polyethylene melts in tapered dies. Int Polym Proc 2010;25:287–96.
[36] Kalogirou A, Poyiadji S, Georgiou GC. Incompressible Poiseuille flows of Newtonian liquids with a pressure-dependent viscosity. J Non-Newtonian Fluid Mech 2011;166:413–9.
[37] Tanner RI. A new inelastic theory of extrudate swell. J Non-Newtonian Fluid Mech 1980;6:289–302.
[38] Mitsoulis E. Extrudate swell in double-layer flows. J Rheol 1986;30(S):S23–44.
[39] Ruschak KJ. A method for incorporating free boundaries with surface tension in finite element fluid-flow simulators. Int J Numer Meth Eng 1980;15:639–48.